Electronic Supporting Information (ESI)

Electrocatalytic Valorization of Bio-based 2,5-Furandicarboxylic Acid: Selective Ring-Opening Hydrogenation to 2-Hydroxyadipic Acid over Nanostructured Bismuth

Ting-Yi Chung[1+], Tzu-Hsuan Wang[1+], Fitri Nur Indah Sari[1], Jie-You Ke[1], Chi-Cheng Chiu[1,2,3,4*], and Chia-Yu Lin[1,2,3*]

[1]Department of Chemical Engineering, National Cheng Kung University, Tainan City 70101, Taiwan
[2]Center for Resilience and Intelligence on Sustainable Energy Research (RiSER), National Cheng Kung University, Tainan 70101, Taiwan.
[3]Fire Protection and Safety Research Center, National Cheng Kung University, Tainan 70101, Taiwan.
[4]Department of Chemical Engineering, Faculty of Engineering, Chulalongkorn University, Bangkok 10330, Thailand.

+ These authors contributed equally.
* Corresponding authors: cyl44@mail.ncku.edu.tw (Prof. C.-Y. Lin), ccchiu2@mail.ncku.edu.tw (Prof. C.-C. Chiu)

Contents

Experimental Section	Page S2
Supporting Table S1-S2	Page S5
Supporting Figures S1–S21	Page S7
References	Page S21

Experimental

Chemicals and Materials. All the chemicals, including 2,5-furandicarboxylic acid (FDCA; 98%, Sigma-Aldrich), tetrahydrofuran-2,5-dicarboxylic acid (THFDCA; 95%, Sigma-Aldrich), 6-hydroxycaproic (HCA; 95%, Alfa Aesar), 2-hydroxyadipic acid (HAA; 98%, Sigma-Aldrich), formic acid (FA; 99.5%, Echo Chemical), 2-furoic acid (2-FA; 98%, Thermo Fisher Scientific), adipic acid (AA; 97%, Acros Organics), bismuth (III) nitrate (>98%, Sigma-Aldrich), sulfuric acid (97%, J.T. Baker), nitric acid (HNO_3; 65%, J.T. Baker), 1,4-Benzoquinone (99.8%, Sigma-Aldrich), potassium iodide (99.5%, Sigma-Aldrich), boric acid (≥99.8%, Sigma-Aldrich), lead(II) nitrate (≥99%, Sigma-Aldrich), acetonitrile (99%, Sigma-Aldrich), ethanol (≥99.5%, Echo Chemical), acetone (99.5%, Echo Chemical), hydrogen chloride (≥37%, Honeywell Fluka™), tetrabutylammonium phosphate (TBAP; 97%, Angene), tetrapropylammonium bromide (TPAB; 99%, Thermo Scientific), tetraethylammonium perchlorate (TEAP; 98%, Alfa Aesar), and Nafion® 117 membrane (Sigma-Aldrich) were purchased from commercial suppliers and used as received. Toray carbon paper (TGP-H-60, Thermo Fisher Scientific) and copper foil (thickness: 0.1 mm; ≥99.99%; Central Research Company, Taiwan) were used as the electrode substrate. Deionized water (18.2 MΩ cm; DIW) was used for rinsing the electrodes and preparing all aqueous electrolyte solutions.

Electrode preparation. Electrochemical preparation of electrode was performed using a CHI 760E potentiostat (CH Instruments, Inc., USA) connected with a customized three-electrode electrochemical cell with carbon paper (exposed area: 1.5 cm^2) as the working electrode, Ag/AgCl (sat'd KCl) as the reference electrode, and Pt foil (1 cm × 4 cm) as the counter electrode. Prior to the electrodeposition process, the carbon paper substrate was cleaned by successive 5-min ultrasonication steps in nitric acid and ethanol, followed by 10 min in DIW, and then air-dried.

The bismuth nanosheet-modified electrode was synthesized by first electrodepositing BiOI nanosheets in the plating solution containing bismuth nitrate (40 mM), potassium iodide (0.4 M), and p-benzoquinone (50 mM) at -0.1 V vs. Ag/AgCl for 4 min, followed by the electrochemical reduction of BiOI nanosheets to bismuth nanosheets in borate buffer (0.1 M, pH 9.2) at -1.2 V vs. RHE for 30 min. The obtained bismuth nanosheet electrode was rinsed with DIW and air-dried.

Physical characterization. The surface morphology of the prepared electrodes was characterized using a Hitachi SU-8010 scanning electron microscope equipped with energy-dispersive X-ray spectroscopy (EDS). Detailed structural analyses were performed by transmission electron microscopy (TEM) and high-resolution transmission electron microscopy (HRTEM) with a JEM-2100F microscope (JEOL Ltd., Japan). The loading amount of Bi species (N_{Bi}) in the prepared electrodes was quantified using a Horiba Jobin Yvon JY 2000-2 ICP-OES. The crystalline structure of the prepared electrodes was analyzed using a Rigaku Ultima IV X-ray diffractometer. The surface oxidation state of the prepared electrode was characterized using X-ray photoelectron spectroscopy (XPS) with a Thermo Fisher- K-Alpha. All XPS spectra were calibrated to the C 1s peak at 284.6 eV.

Electrochemical characterization. All measurements were conducted at room temperature (~25 °C) and ambient pressure. The electrocatalytic properties of the prepared electrodes towards the electrocatalytic FDCA reduction reaction (*e*-FDCArr) were characterized in the custom-made H-cell connected to a CHI 760E potentiostat (CH Instruments, Inc., USA). The anodic and cathodic compartments of the H-cell were separated with a Nafion® 117 ion exchange membrane. The prepared electrodes were used as the working electrode and placed with an Ag/AgCl (sat'd KCl) reference electrode in the cathodic compartment, while the Pt counter electrode was placed in the anodic compartment. The electrolysis was carried out in the de-aerated H_2SO_4 solution (0.1 M) containing FDCA (2.5 mM) and specific quaternary ammonium salt (QAS) under the purge of N_2 gas (99.99%; Yun Shan Gas Co., Taiwan) with 100% IR compensation. For performance comparison, electrolysis experiments were also performed using bare carbon paper as the working electrode in the H_2SO_4 solutions containing Bi^{3+} ions of different concentrations (0 ppm and 20 ppm), FDCA (2.5 mM), and TBAP (30 mM). The electrode obtained from the 2-h electrolysis in H_2SO_4 solution

containing Bi^{3+} ions (20 ppm), FDCA (2.5 mM), and TBAP (30 mM) was designated as *e*-Bi electrode. All the applied potentials were reported against the RHE by using Eq. 1:

E (V vs. RHE) = E (V vs. Ag/AgCl) + 0.197 + 0.059×pH (1)

The amount of electrochemically available bismuth species (*e*-N_{Bi}) on the prepared electrodes was determined by firstly estimating the charge responsible for the Bi^0/Bi^{3+} redox reactions via the integration of the area under the corresponding redox peaks in cyclic voltammograms (scan rate: 100 mV s^{-1}), followed by converting the estimated charge into moles of bismuth species using Faraday's law.

To evaluate the influence of the electrolyte on *e*-FDCArr performance, several supporting electrolytes were investigated, including NH_4Cl (0.1 M, pH 3), Na_2SO_4 (0.1 M, pH 5), and phosphate buffer (0.1 M, pH 7). The pH values were adjusted using 1 M H_2SO_4 or 1 M NaOH as required.

Product analysis. Liquid products, including THFDCA, HAA, FA, AA, HCA, and 2-FA generated from the electrolysis, were analyzed and quantified using a Shimadzu Nexera-I LC-2040C 3D high-performance liquid chromatography system (HPLC) equipped with a Shodex SUGAR SH1821 column, a photodiode array (PDA) detector, and a refractive index detector (RID). THFDCA, HAA, HCA, and 2-FA were quantified using the PDA detector (λ = 207 nm), whereas FA and AA were quantified using the RID detector. HPLC analysis was conducted at 60 °C using a H_2SO_4 aqueous solution (2 mM) as the eluent at a flow rate of 0.6 mL min^{-1}. To verify product identities, Ultraperformance Liquid Chromatography-Tandem Quadrupole Mass Spectrometry (UHPLC-MS) analyses were also performed with a system consisting of a Thermo Scientific™ Dionex Ultimate™ 3000 UHPLC system and a Q Exactive™ Plus Hybrid Quadrupole-Orbitrap™ Mass Spectrometer. Electrospray ionization with a positive polarity ($[M+H]^+$) mode was used as an ion source, and the analysis was performed in full mass range, which tracks products ranging from m/z of 90 Da–1000 Da. The ionization parameters were adjusted as follows: spray voltage: 1.5 kV; sheath gas pressure: 35 psi; aux gas pressure: 10 psi. Concurrently, H_2 generated from CCE experiments was quantified using an Agilent 7890A Series gas chromatography (GC) equipped with a thermal conductivity detector (TCD) and HP-PLOT Molesieve column. The GC oven was held at 40 ºC for 8 min, and ramped at a rate of 40 ºC/min to 200 ºC, and maintained at 200 °C for 6 min. The amounts of generated products (N_p) were determined by converting the measured HPLC and GC signals with routinely updated calibration curves (**Figure S1)**. The charge consumed (Q_p) and corresponding faradaic efficiency (FE_p) for the formation of these four products were then determined, respectively, using Eq. 2 and Eq. 3:

$$Q_p = N_p \times n \times F \qquad (2)$$

$$FE_p = \frac{Q_p}{Q_{total}} \times 100\% \qquad (3)$$

where n is the number of electrons transferred, F is the Faradaic constant (96,485 C mol^{-1}), and Q_{total} is the total charge passed in each electrolysis experiment. The FDCA conversion (χ_{FDCA}), product selectivity (S_p), and product yield (Y_p) were calculated using Eqs. 4-6:

$$\chi_{FDCA}(\%) = \frac{N_{FDCA,0} - N_{FDCA}}{N_{FDCA,0}} \times 100\% \quad (4)$$

$$S_p(\%) = \frac{N_p}{N_{FDCA,0} - N_{FDCA}} \times 100\% \qquad (5)$$

$$Y_p(\%) = \frac{N_p}{N_{FDCA,0}} \times 100\% \qquad (6)$$

where $N_{FDCA,0}$ and N_{FDCA} represent the initial and final amounts of FDCA, respectively. Turnover frequency for HAA production (TOF_{HAA}), defined as the ratio of HAA production rate (R_{HAA}) to the

ICP-OES-quantified loading amount of bismuth species (N_{Bi}), was used to evaluate the overall electrocatalytic activity of the prepared electrodes.

Density functional theory (DFT) calculations. Spin-polarized DFT calculations were conducted using the DMol^3 module within BIOVIA Materials Studio. The hybrid meta-GGA functional M06-2X was adopted to accurately account for exchange–correlation interactions, as it accurately describes main-group thermochemistry and noncovalent interactions.[1] All atoms were described using the DNP 4.4 basis set (double numerical plus polarization). Geometric optimizations were performed without symmetry constraints, employing convergence thresholds of 2×10^{-3}Ha Å^{-1} for energy, 1×10^{-3} Ha for maximum force, and 1×10^{-3} Å for maximum displacement. The self-consistent field tolerance was tightened to 1.0×10^{-6} Ha, utilizing a fine numerical integration grid to ensure accurate and stable convergence. Solvent effects in an aqueous environment ($\varepsilon = 78.54$) were accounted for via the Conductor-like Screening Model. Finally, vibrational frequency analyses were performed to verify that all the optimized geometries represent local minima, characterized by the absence of imaginary frequencies. Spin polarization was enabled for all calculation involving open-shell species.

Molecular dynamics (MD) simulations. All-atom MD simulations were performed using the GROMACS 2016 package to investigate the interfacial behavior of FDCA and various quaternary ammonium salts (QAS). Inter- and intramolecular interactions were described by the OPLS force field.[2] The initial configuration of the simulated system was constructed using PACKMOL,[3] comprising 10 FDCA molecules, 120 QAS cations (TEA, MBA, or TBA), and 120 Br^- counter-ions. These components were confined within a simulation box ($5.16 \times 5.10 \times 30$ nm^3) between two graphene layers (5.16×5.10 nm^2), each containing 1008 atoms, to model the electrochemical interface. To mimic the cathodic environment, a partial charge of ± 0.01 *e* was assigned to each graphene atom, resulting in a constant surface charge density of 0.06 C m^{-2}.

The simulation started with energy minimization using the steepest descent algorithm to remove any close atomic overlaps, followed by 1 ns equilibration run in the NVT ensemble (constant volume and constant temperature) at 300 K. The inter-layer distance of graphene layers was adjusted to e to match bulk solvent density. Subsequently, a 100 ns production run was performed at 300 K in the NVT ensemble, with trajectories recorded every 10 ps for analysis.

Periodic boundary conditions were applied in all three dimensions. Van der Waals (vdW) and short-range electrostatic interactions were truncated at a cutoff distance of 1.2 nm, with vdW forces smoothly shifted to zero starting from 0.9 nm. Long-range electrostatic interactions were computed using the Particle Mesh Ewald algorithm.[4-5] The system temperature was regulated using the Nose-Hoover thermostat with a coupling time constant of 0.1 ps.[6-7] System configurations and trajectories were visualized and analyzed using the Visual Molecular Dynamics software and GROMACS built-in modules, supplemented by custom scripts for the determination of molecular adsorption orientation.[8-9]

Table S1 Summary of minor products from 2-h electrolysis at -10 mA cm^{-2} in the presence of TBAP of various concentrations using the bismuth nanosheet electrode.

C_{TABP} (mM)	Product	N_p (μmole cm^{-2})	FE_p (%)	S_p (%)	Y_p (%)
0	HCA	0.00	0.00	0.00	0.00
	2-FA	0.00	0.00	0.00	0.00
	AA	0.00	0.00	0.00	0.00
10	HCA	0.11	0.15	0.26	0.18
	2-FA	0.01	0.00	0.03	0.02
	AA	0.00	0.00	0.00	0.00
20	HCA	0.17	0.23	0.34	0.28
	2-FA	0.03	0.00	0.06	0.05
	AA	0.05	0.06	0.10	0.08
30	HCA	0.22	0.30	0.43	0.37
	2-FA	0.02	0.00	0.04	0.03
	AA	0.07	0.07	0.13	0.11
50	HCA	0.55	0.74	1.22	0.94
	2-FA	0.05	0.01	0.12	0.09
	AA	0.07	0.07	0.14	0.11

Table S2 Optimized intermediate structure formed during ECH and ring-opening of FDCA.

Path	[FDCA]$^-$	int 1	int 1’
(i)		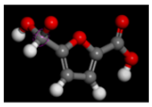	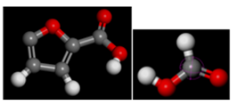
(ii)			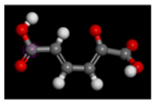
(iii)	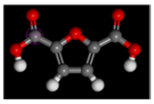	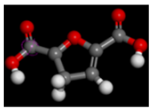	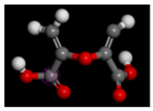
(iv)		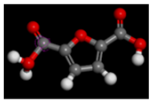	
(v)			
(vi)		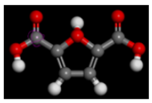	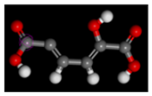
(vi’)	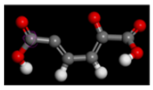		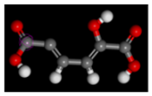

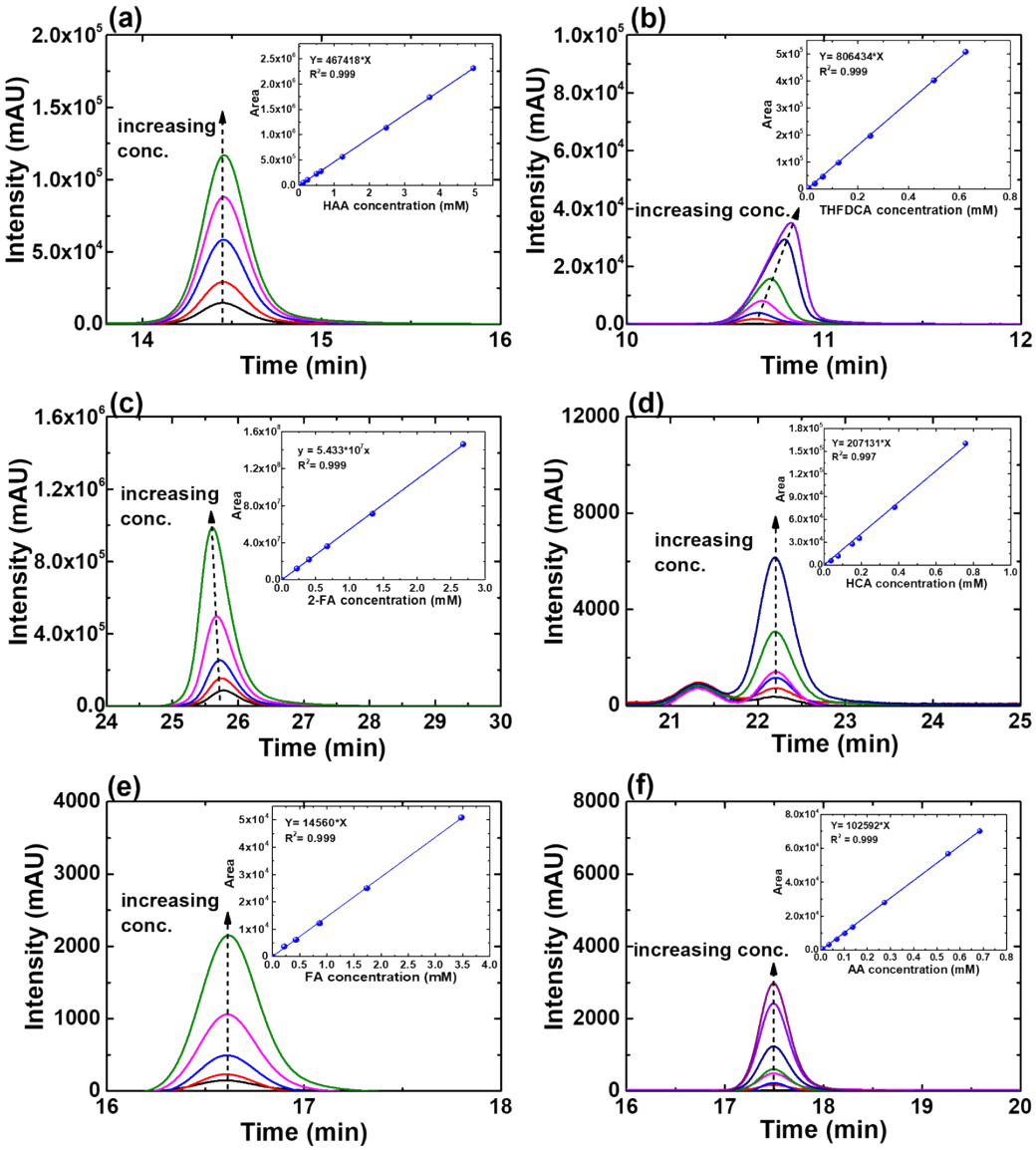

Figure S1. HPLC chromatograms and corresponding calibration curves for the detected products: (a) HAA, (b) THFDCA, (c) 2-FA, (d) HCA, (e) FA, and (f) AA.

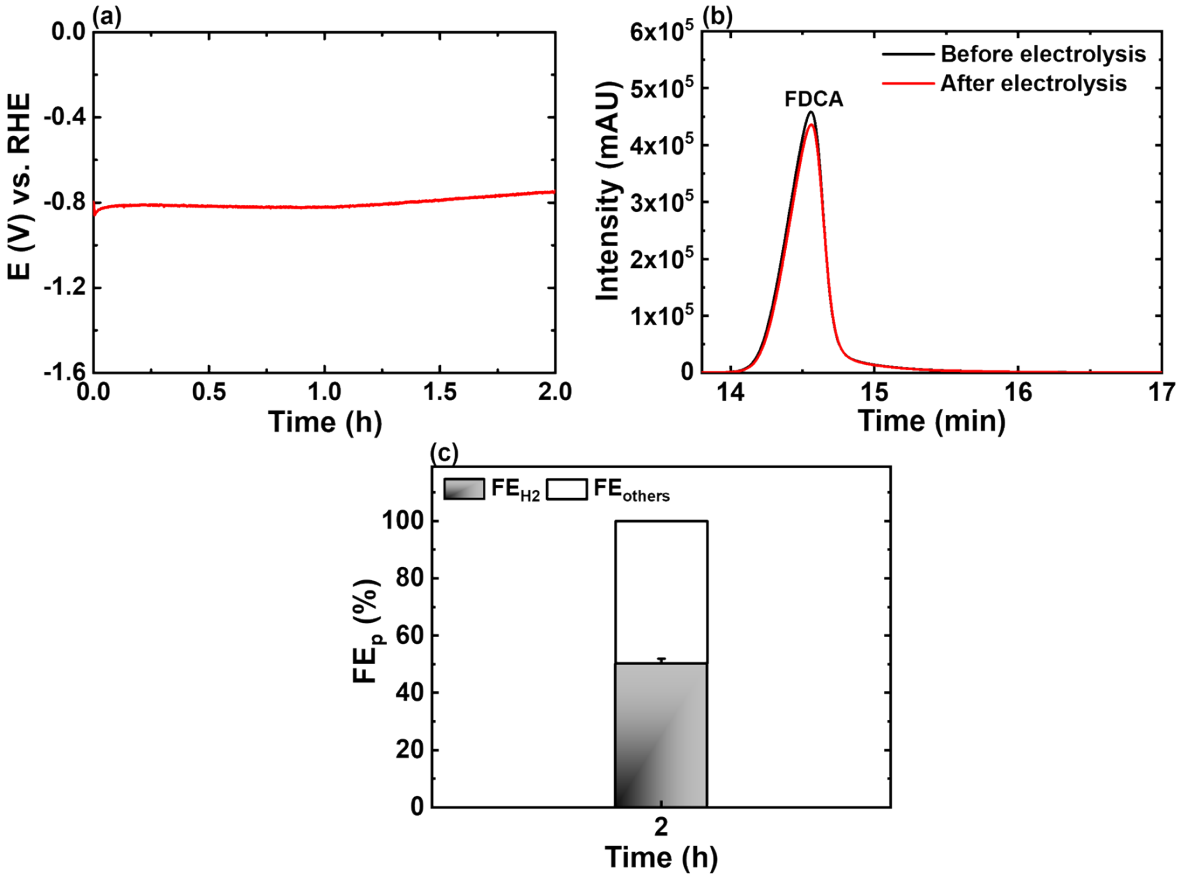

Figure S2. *e*-FDCArr performance of the carbon paper obtained from 2-h electrolysis at -10 mA cm^{-2} in H_2SO_4 solution (0.1 M) containing TBAP (30 mM) and FDCA (2.5 mM). (a) Potential transient obtained during 2-h electrolysis. (b) HPLC chromatograms of the electrolyte recorded before and after electrolysis. (c) FE_p.

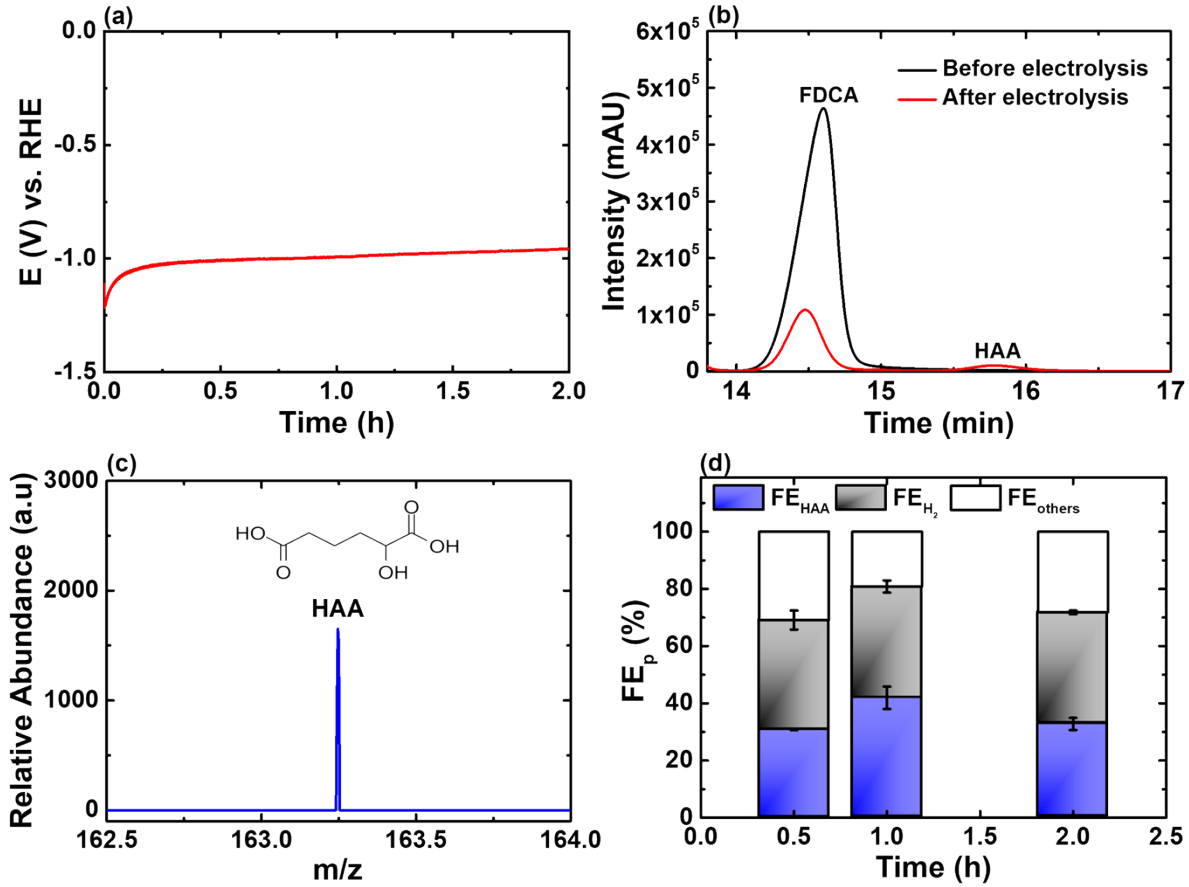

Figure S3. *e*-FDCArr performance of the carbon paper electrode obtained from 2-h CCE at -10 mA cm^{-2} in H_2SO_4 solution (0.1 M) containing Bi^{3+} ions (20 ppm), TBAP (30 mM), and FDCA (2.5 mM). (a) Potential transient obtained during 2-h electrolysis. (b) HPLC chromatograms of the electrolyte recorded before and after electrolysis. (c) Mass spectrum of the product corresponding to the HAA peak identified in (b). Inset: chemical structure of HAA. (d) FE_p.

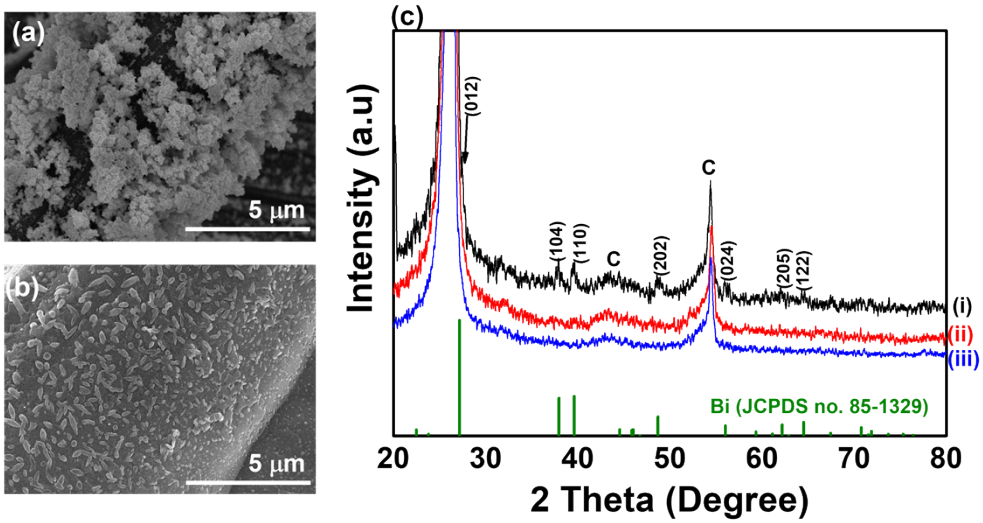

Figure S4. Morphological and structural characterization. (a, b) SEM images of the carbon paper after 2-h electrolysis at -10 mA cm^{-2} in H_2SO_4 solutions containing (a) Bi^{3+} ions (20 ppm) and (b) Bi^{3+} ions (20 ppm) and TBAP (30 mM). (c) performance of the bare carbon paper electrode. (c) XRD patterns of the carbon paper electrodes obtained after 2-h electrolysis at -10 mA cm^{-2} in H_2SO_4 solutions (0.1 M) containing (i) Bi^{3+} ions (20 ppm), (ii) Bi^{3+} ions (20 ppm) and TBAP (30 mM), and (iii) Bi^{3+} ions (20 ppm), TBAP (30 mM), and FDCA (2.5 mM).

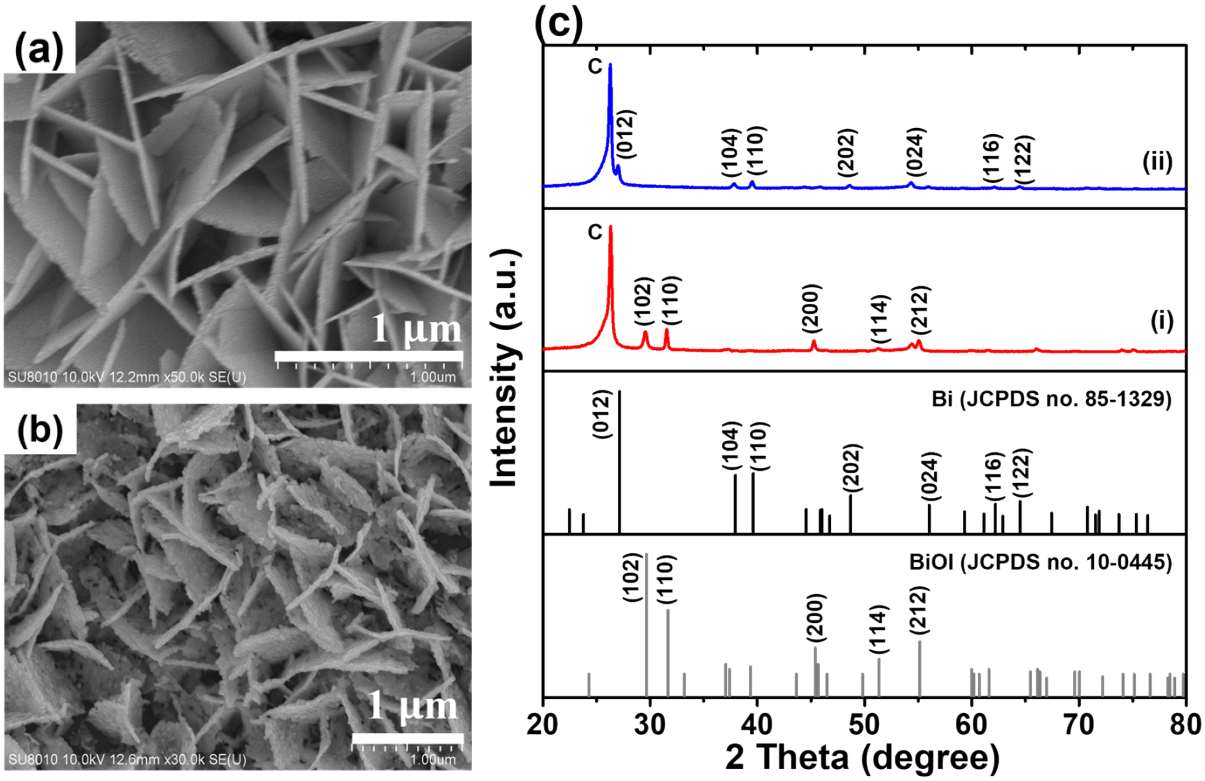

Figure S5. Morphological and structural transformation from BiOI template to nanoBi. (a, b) SEM images of the carbon paper electrode (a) after electrodeposition of the BiOI nanosheet template and (b) following electrochemical reduction to the metallic nanoBi. (c) XRD patterns confirming the phase transition from (i) the tetragonal BiOI phase (JCPDS no. 10-0445) to (ii) the rhombohedral metallic Bi phase (JCPDS no. 85-1329).

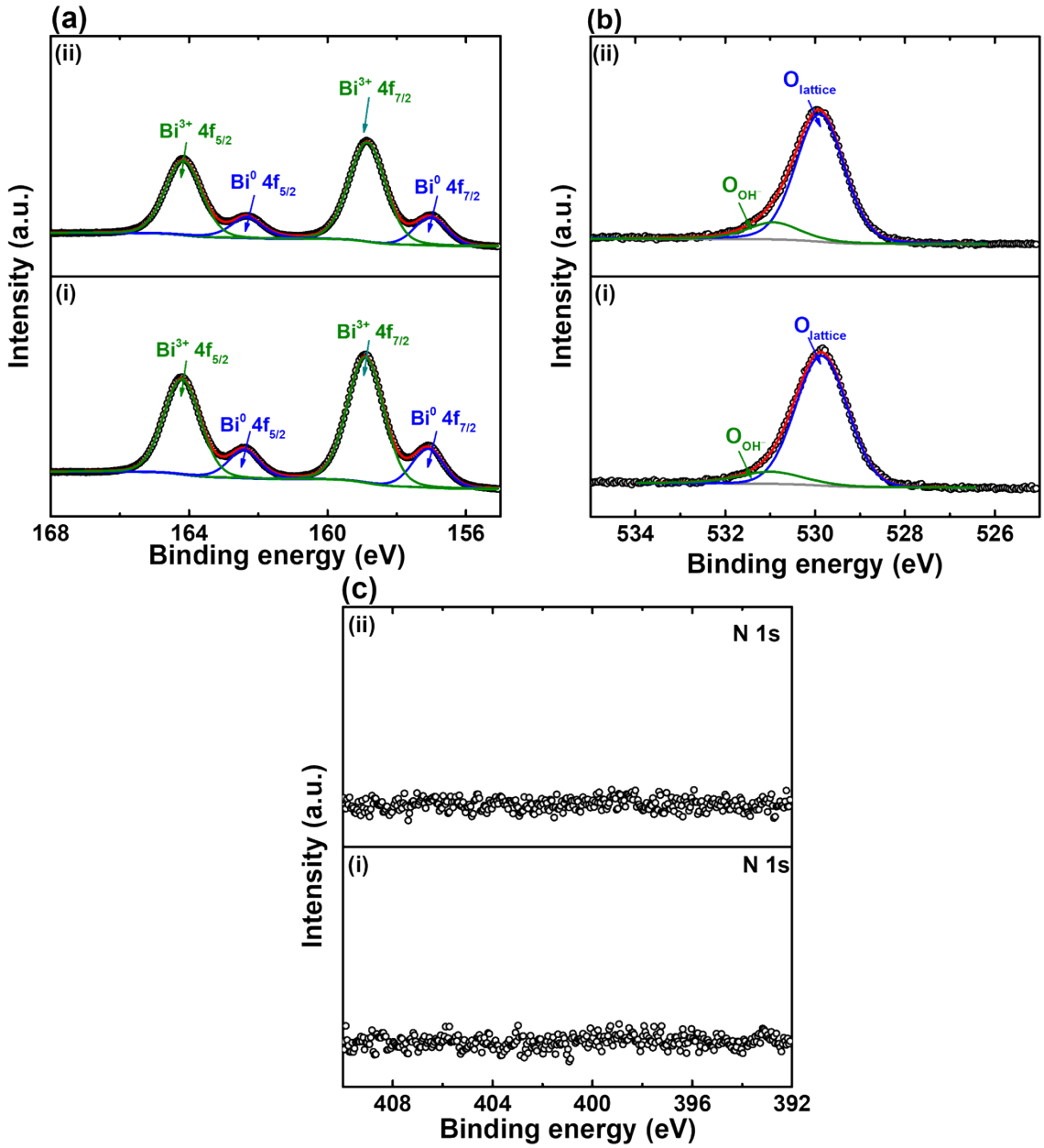

Figure S6. XPS spectra of the bismuth nanosheet electrode (i) before and (ii) after 2-h electrolysis in 0.1 M H_2SO_4 containing 30 mM TBAP and 2.5 mM FDCA. Panels correspond to the (a) Bi 4f, (b) O 1s, and (c) N 1s regions.

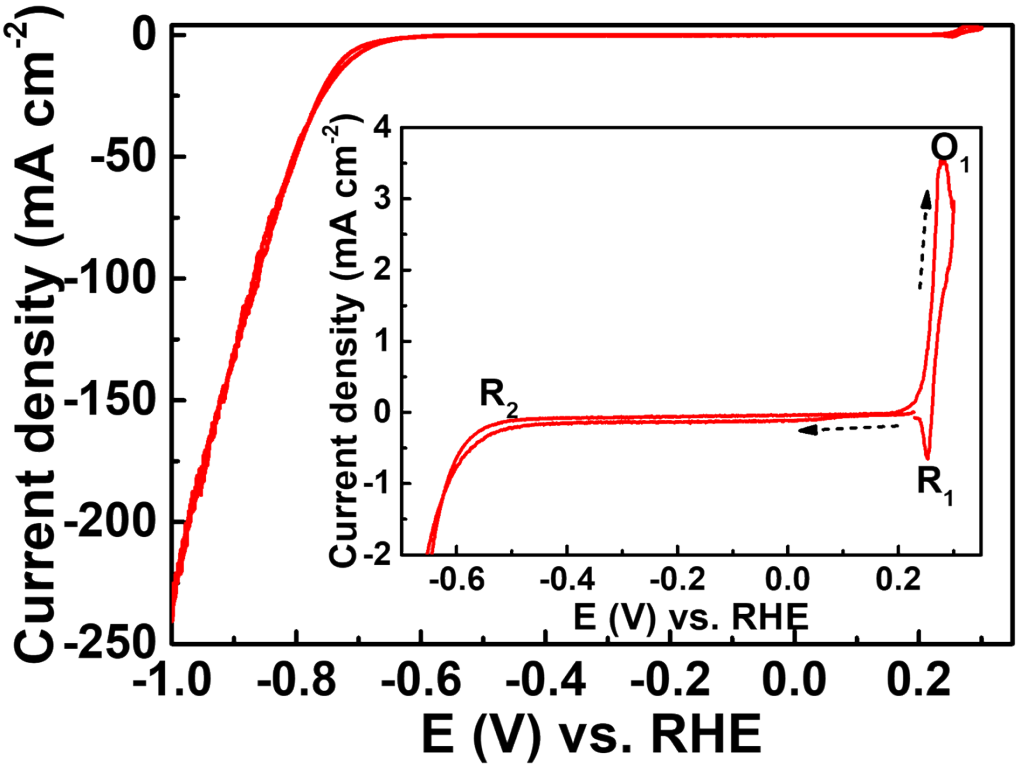

Figure S7. Cyclic voltammogram (CV) of the as-prepared bismuth nanosheet electrode in 0.1 M H_2SO_4 at a scan rate of 10 mV s^{-1}. The inset provides an enlargement of the CV within the potential range of 0.35 to -0.7 V vs. RHE.

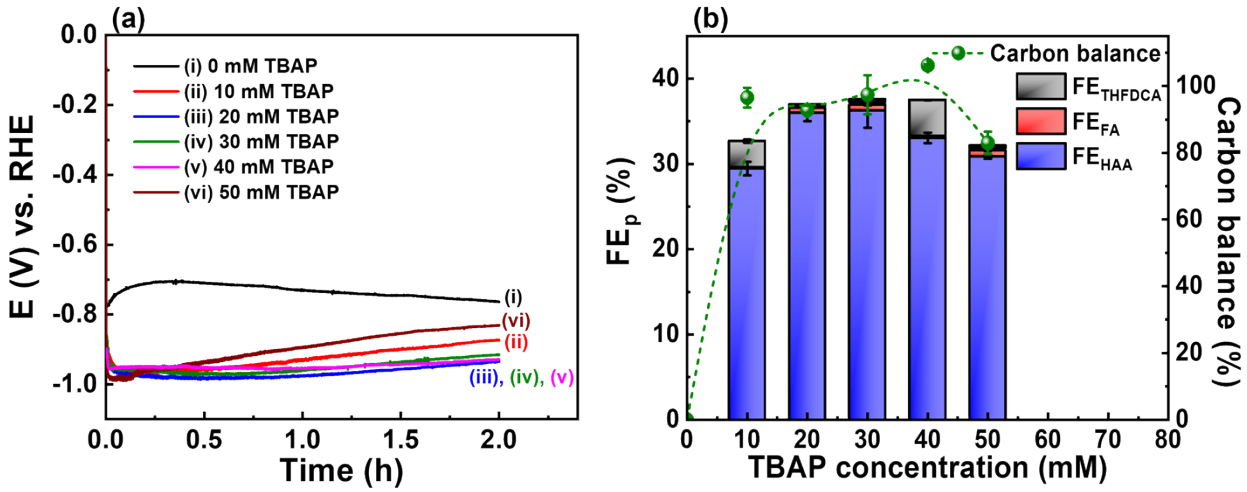

Figure S8. *e*-FDCArr performance of the Bi nanosheet electrode obtained from 2-h electrolysis at -10 mA cm^{-2} in H_2SO_4 solution (0.1 M) containing TBAP (0-50 mM) and FDCA (2.5 mM). (a) Potential transient obtained during 2-h electrolysis. (b) FE_p and corresponding carbon balances.

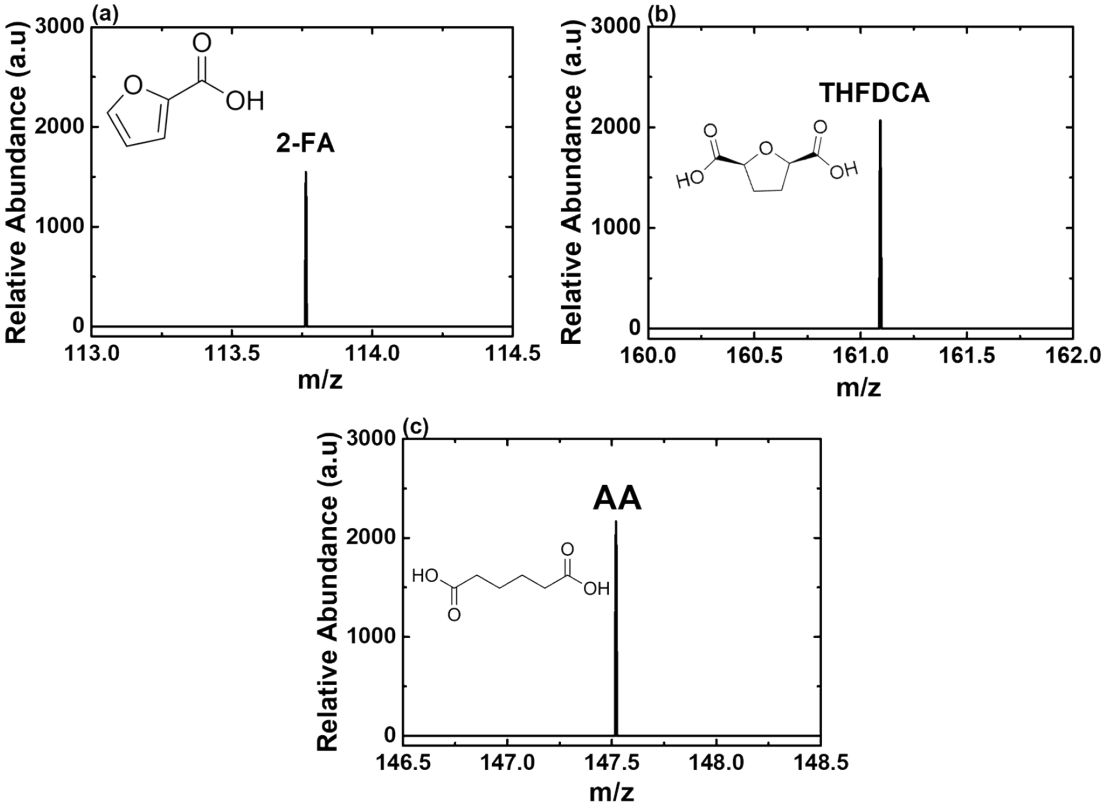

Figure S9. Mass spectrometric identification of reaction products. High-resolution mass spectra of the peaks corresponding to (a) 2-FA, (b) THFDCA, and (c) AA, as identified in the HPLC analysis. The insets in (a), (b), and (c) display the corresponding chemical structures for each identified species.

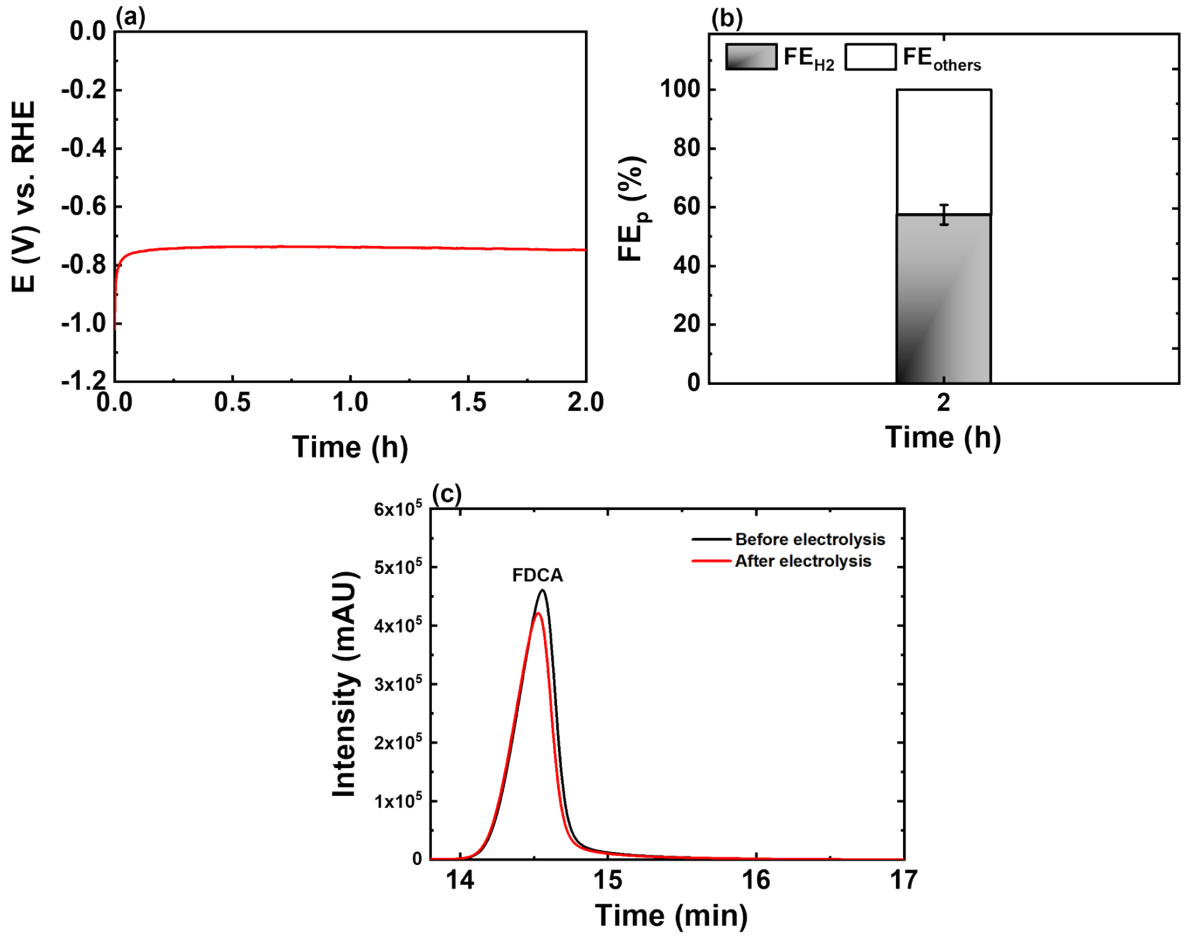

Figure S10. *e*-FDCArr performance of the carbon paper electrode obtained from 2-h electrolysis at -10 mA cm^{-2} in H_2SO_4 solution (0.1 M) containing Bi^{3+} ions (20 ppm) and FDCA (2.5 mM). (a) Potential transient obtained during 2-h electrolysis. (b) FE_p. (c) HPLC chromatograms of the electrolyte recorded before and after electrolysis.

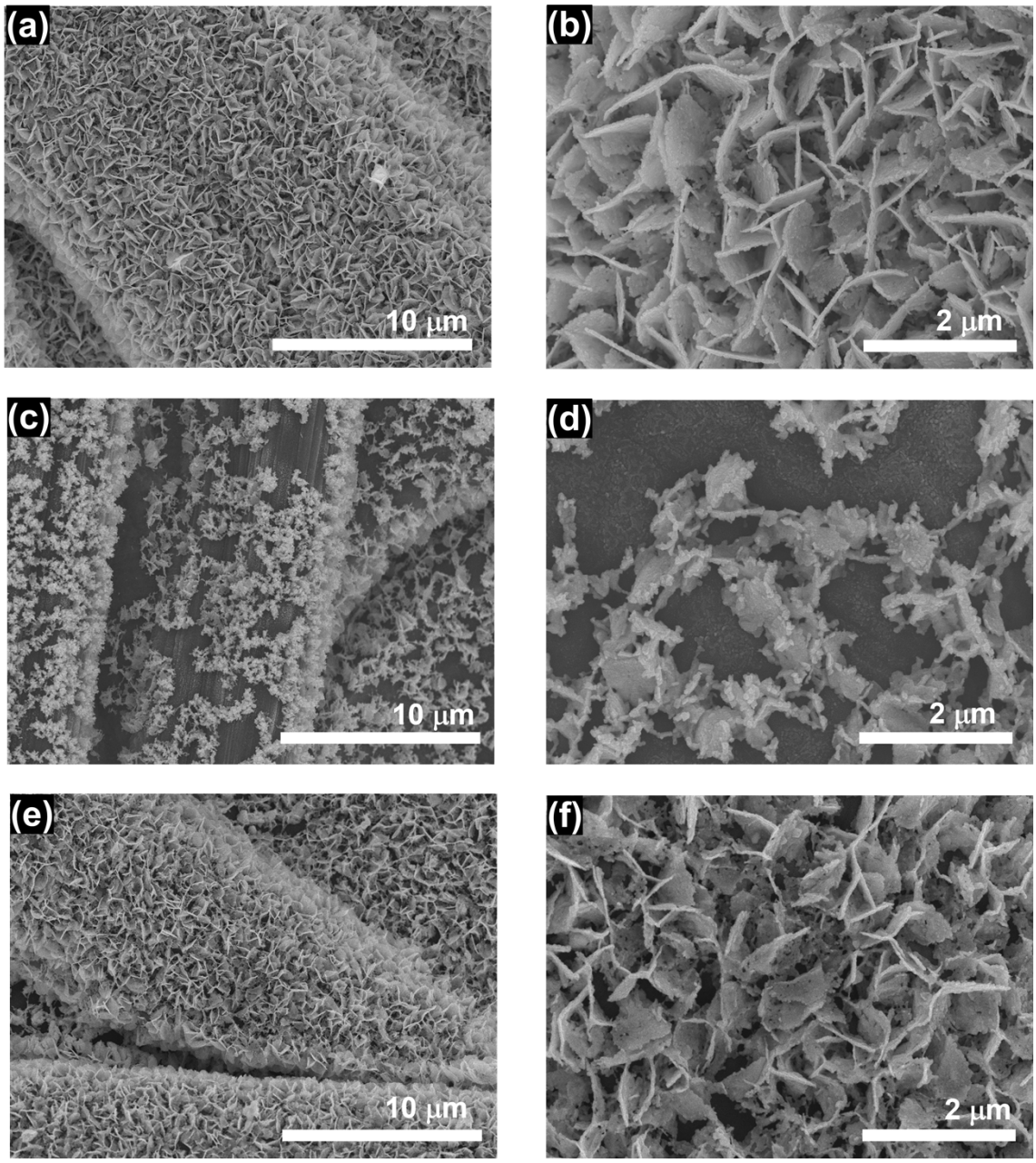

Figure S11. Morphological stability of the bismuth nanosheet electrode. SEM images of (a, b) the as-prepared bismuth nanosheet electrode, compared with the bismuth nanosheet electrodes after 2-h electrolysis at -10 mA cm^{-2} in (c, d) H_2SO_4 solution (0.1 M) containing FDCA (2.5 mM), and (e, f) H_2SO_4 solution (0.1 M) containing TBAP (30 mM) and FDCA (2.5 mM).

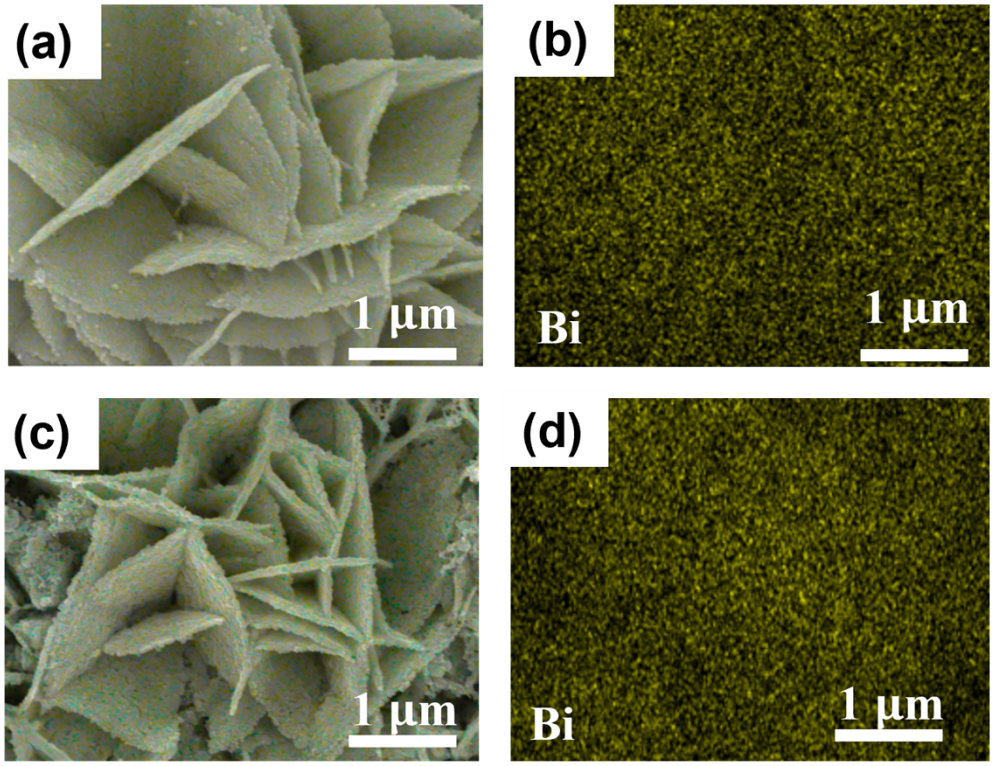

Figure S12. SEM-EDS elemental mapping of the bismuth nanosheet electrode (a-b) before and (c-d) after 2-h electrolysis in 0.1 M H_2SO_4 containing 30 mM TBAP and 2.5 mM FDCA.

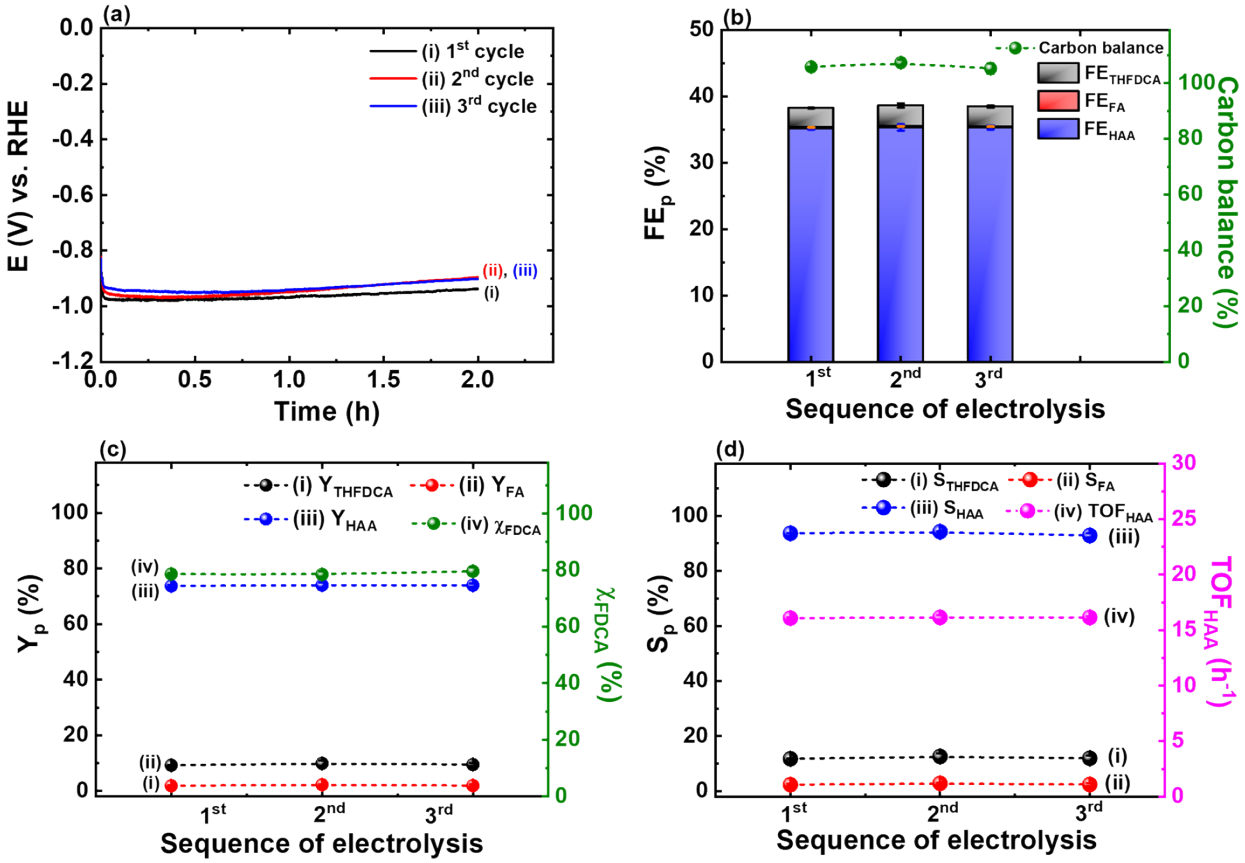

Figure S13. Stability and performance of bismuth nanosheetectrodes for e-FDCArr during three consecutive 2-h electrolysis cycles at -10 mA cm^{-2} in H_2SO_4 solution (0.1 M) containing FDCA (2.5 mM) and TBAP (30 mM). (a) Potential transients, (b) FE_p and corresponding carbon balance, (c) Y_p and χ_{FDCA}, and (d) S_p and TOF_{HAA}. For each subsequent cycle, the electrode was rinsed with deionized water and introduced into a fresh electrolyte solution.

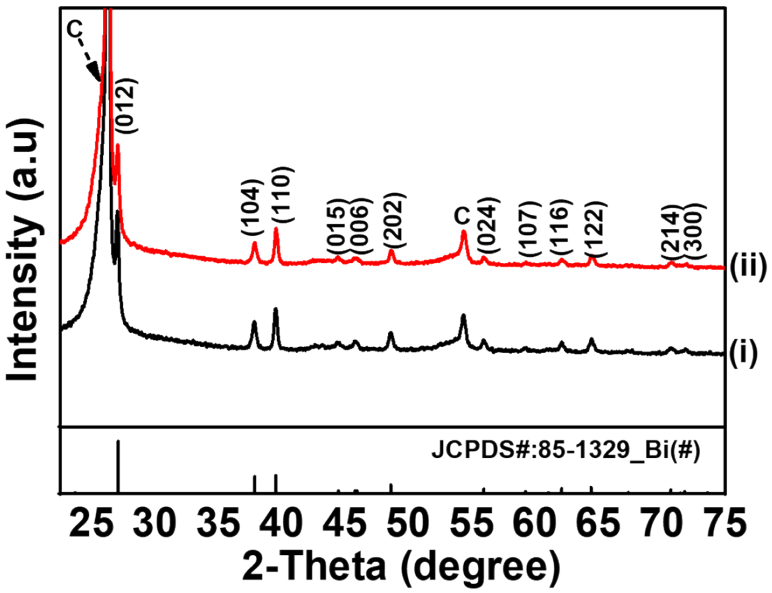

Figure S14. XRD patterns of the bismuth nanosheet electrode (i) before and (ii) after 2-h electrolysis in 0.1 M H_2SO_4 containing 30 mM TBAP and 2.5 mM FDCA.

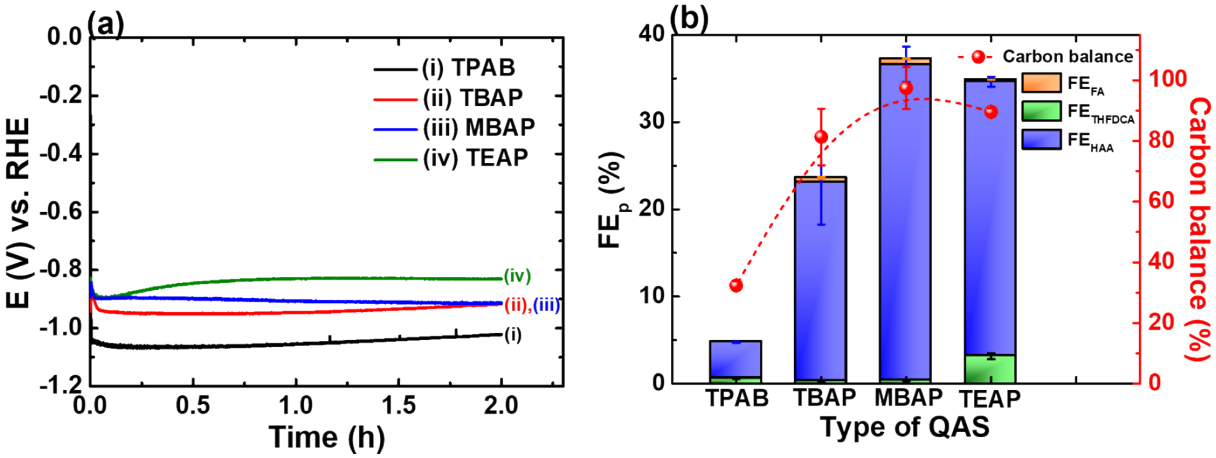

Figure S15. *e*-FDCArr performance of the bismuth nanosheet electrode obtained from 2-h electrolysis at -10 mA cm^{-2} in H_2SO_4 solution (0.1 M) containing FDCA (2.5 mM) and various QAS salts. (a) Potential transient obtained during 2-h electrolysis. (b) FE_p and corresponding carbon balances.

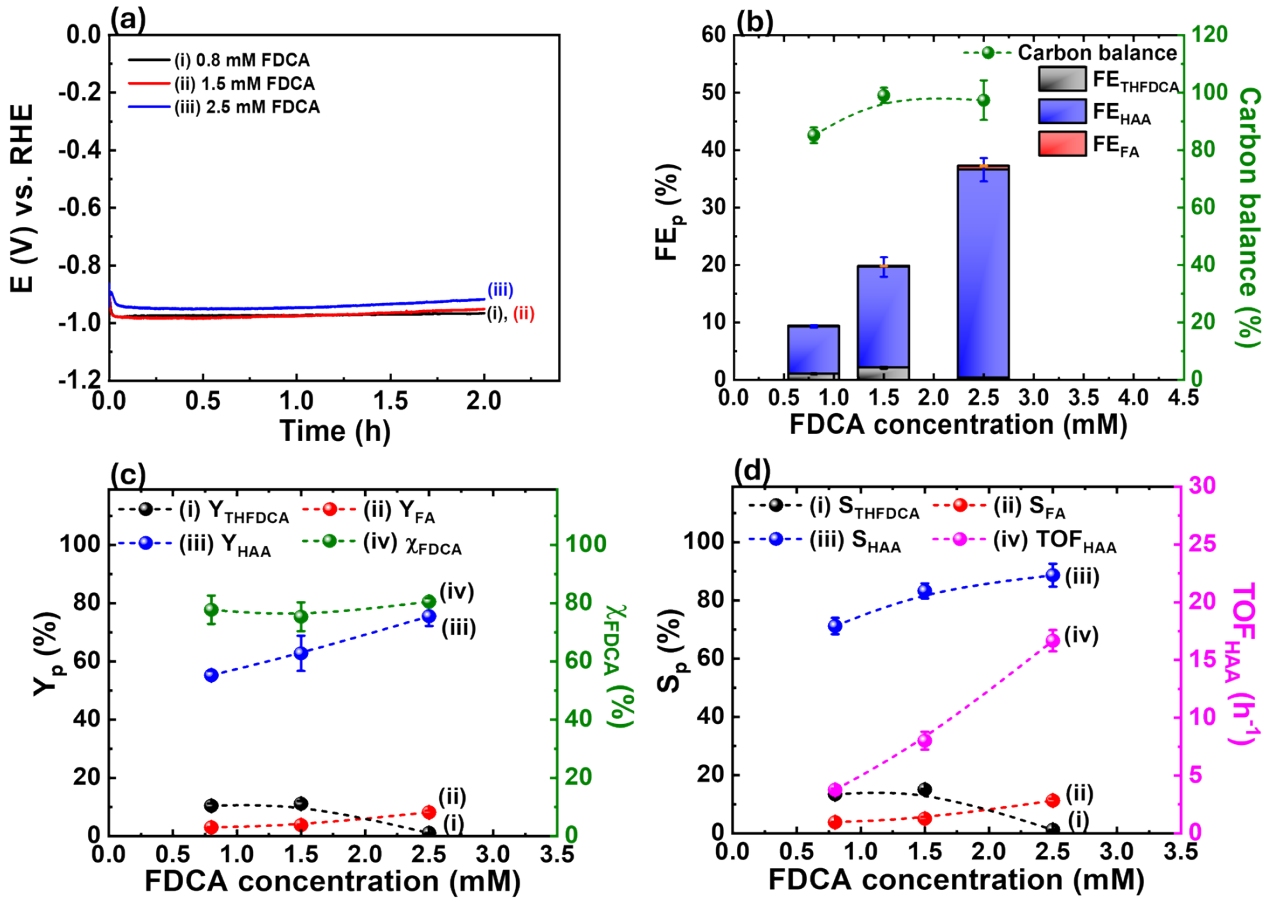

Figure S16. *e*-FDCArr performance of the bismuth nanosheet electrode obtained from 2-h electrolysis at -10 mA cm^{-2} in H_2SO_4 solution (0.1 M) containing various FDCA concentrations (0.8-2.5 mM) and TBAP (30 mM). (a) Potential transients, (b) FE_p and corresponding carbon balance, (c) Y_p and χ_{FDCA}, and (d) S_p and TOF_{HAA}.

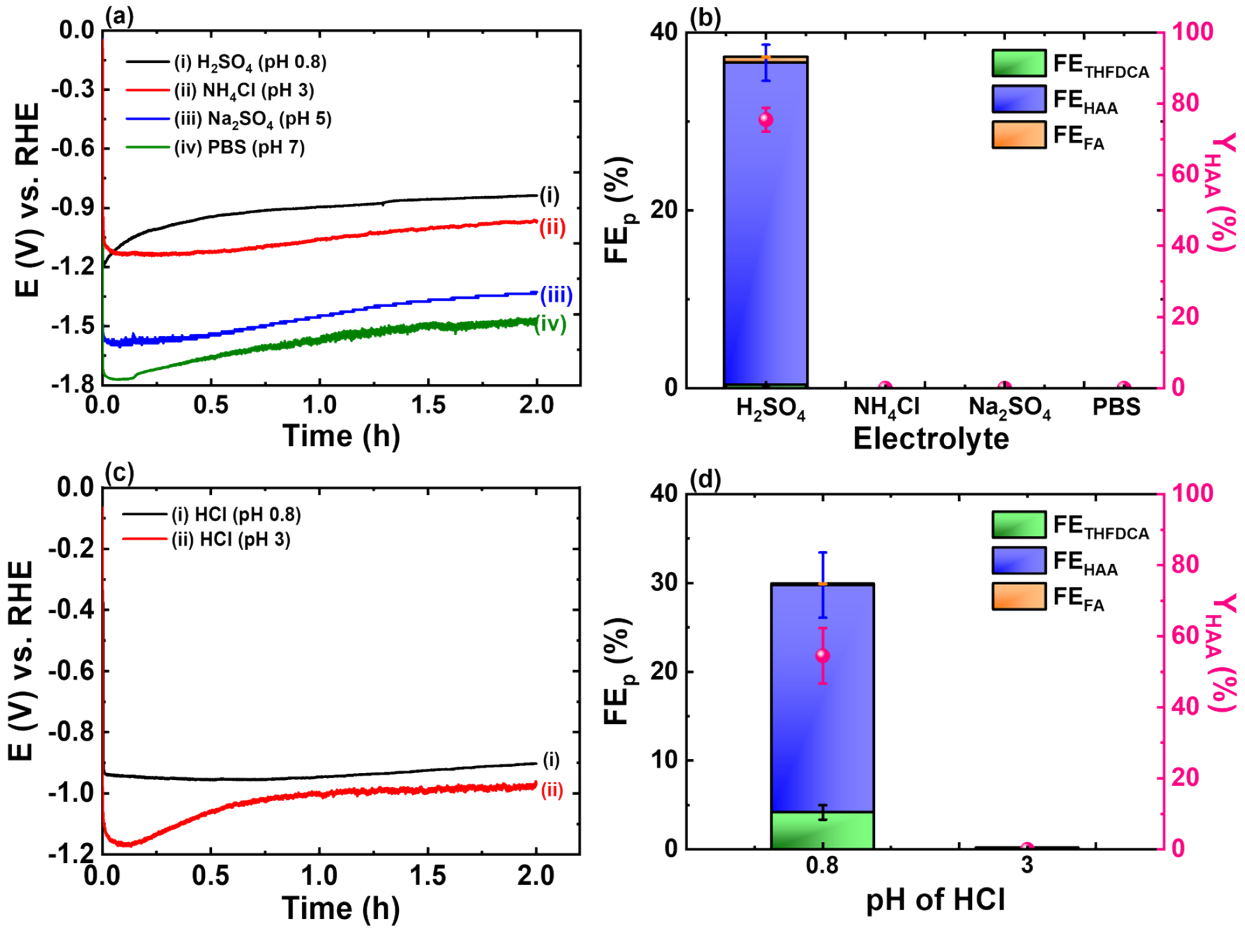

Figure S17. (a-b) Effect of electrolyte pH on the *e*-FDCArr performance of the bismuth nanosheet electrode. Data were collected from 2-h electrolysis at -10 mA cm^{-2} in various electrolyte solutions (0.1 M, pH range 0.8~7.0) containing TBAP (30 mM) and FDCA (2.5 mM). (a) Potential transient obtained during 2-h electrolysis. (b) FE_p and Y_{HAA}. (c-d) Influence of pH on the *e*-FDCArr performance of the bismuth nanosheet electrode. Experiments were conducted at -10 mA cm^{-2} for 2 h in 0.1 M HCl (pH= 0.8 and pH= 3) containing TBAP (30 mM) and FDCA (2.5 mM). (c) Potential transients and (d) corresponding FE_p and Y_{HAA}.

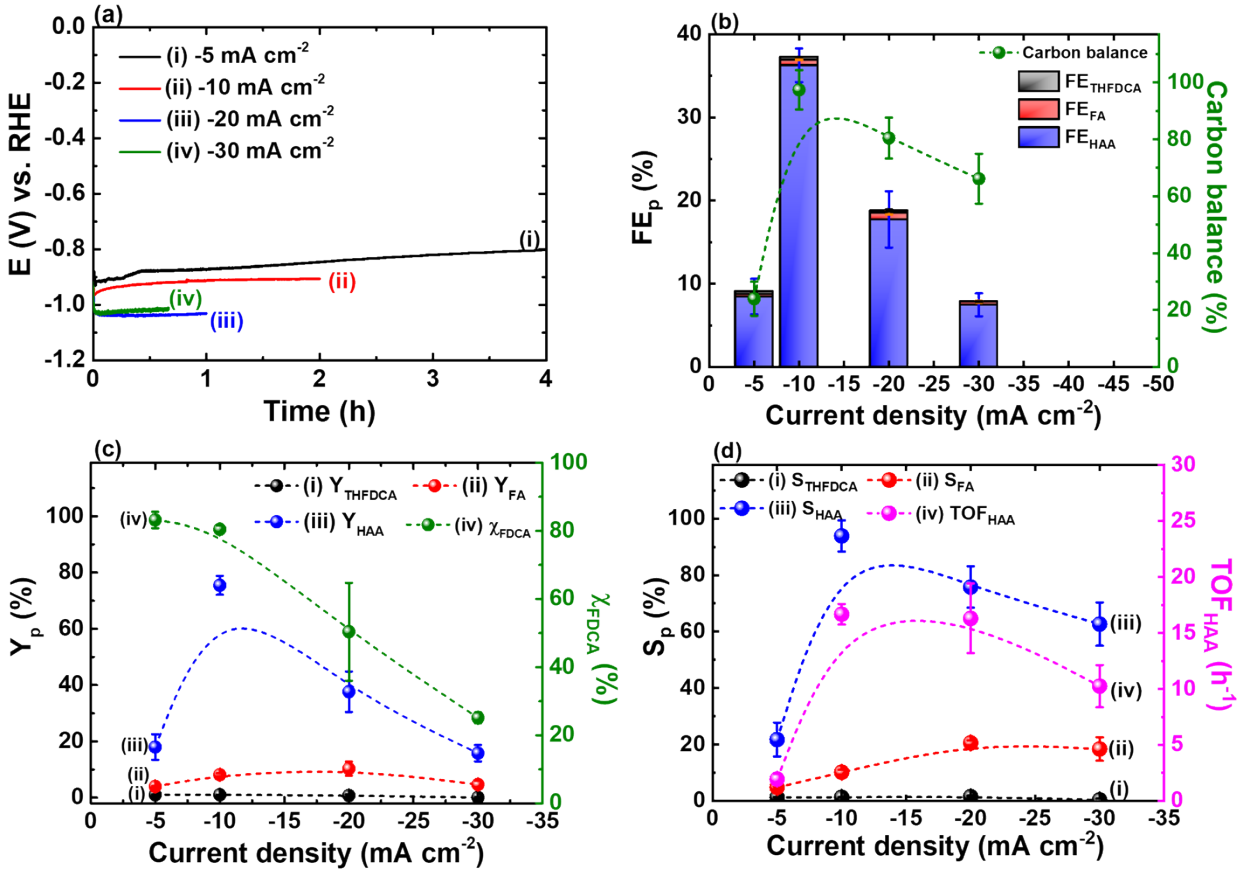

Figure S18. Effect of current density on the *e*-FDCArr performance of the Bi nanosheet electrode. Data were obtained from 2-h electrolysis at various current densities in H_2SO_4 solution (0.1 M) containing TBAP (30 mM) and FDCA (2.5 mM). (a) Potential transients. (b) FE_p and corresponding carbon balance. (c) Y_p and χ_{FDCA}. (d) S_p and TOF_{HAA}.

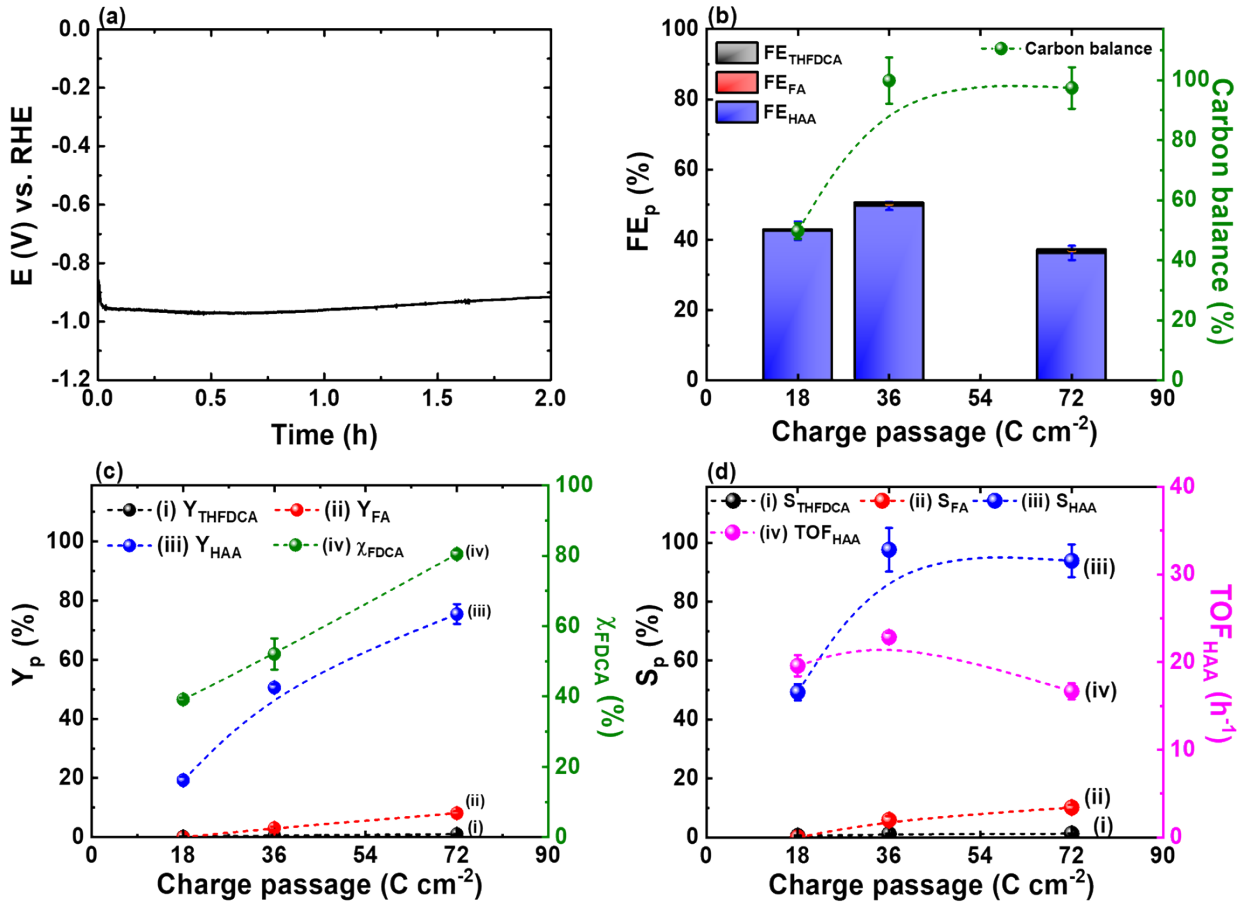

Figure S19. Effect of charge passage on the *e*-FDCArr performance of the Bi nanosheet electrode. Data were obtained from 2-h electrolysis at -10 mA cm^{-2} in H_2SO_4 solution (0.1 M) containing TBAP (30 mM) and FDCA (2.5 mM). (a) Potential transients. (b) FE_p and corresponding carbon balance. (c) Y_p and χ_{FDCA}. (d) S_p and TOF_{HAA}.

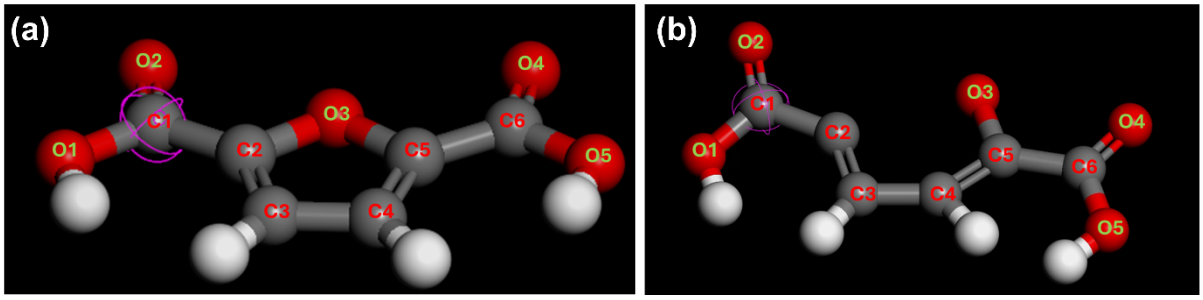

Figure S20. Geometric configurations of FDCA for DFT analysis. Schematic representations of (a) Structure I and (b) Structure II, illustrating the labeling of carbon and oxygen atoms utilized to calculate the free energy barriers for site-specific hydrogenation and ring-opening.

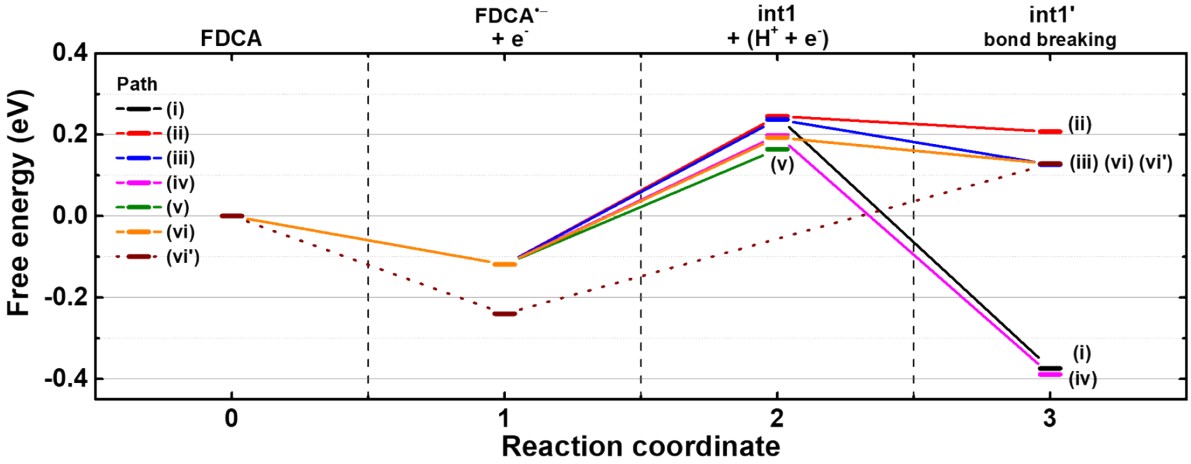

Figure S21. Energetics of FDCA hydrogenation and ring cleavage. Calculated free energy profiles for the site-specific ECH and ring-opening of FDCA, highlighting the potential-dependent energy barriers for each reaction step.

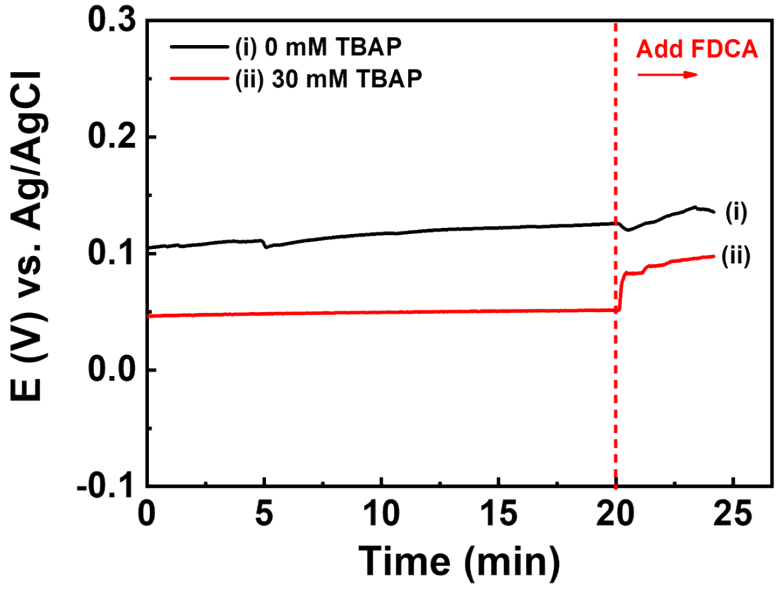

Figure S22. Open-circuit potential (OCP) transients in H_2SO_4 solution (0.1 M) containing (i) 0 M TBAP and (ii) 30 mM TBAP. FDCA was introduced at t= 20 min following OCP stabilization.

References:

[1] Y. Zhao, D. G. Truhlar, "Exploring the Limit of Accuracy of the Global Hybrid Meta Density Functional for Main-Group Thermochemistry, Kinetics, and Noncovalent Interactions" *J. Chem. Theory Comput.* **2008**, *4*, 1849-1868.

[2] W. L. Jorgensen, D. S. Maxwell, J. Tirado-Rives, "Development and Testing of the OPLS All-Atom Force Field on Conformational Energetics and Properties of Organic Liquids" *J. Am. Chem. Soc.* **1996**, *118*, 11225-11236.

[3] L. Martínez, R. Andrade, E. G. Birgin, J. M. Martínez, "PACKMOL: A package for building initial configurations for molecular dynamics simulations" *J. Computat. Chem.* **2009**, *30*, 2157-2164.

[4] T. Darden, D. York, L. Pedersen, "Particle mesh Ewald: An N·log(N) method for Ewald sums in large systems" *J. Chem. Phys.* **1993**, *98*, 10089-10092.

[5] U. Essmann, L. Perera, M. L. Berkowitz, T. Darden, H. Lee, L. G. Pedersen, "A smooth particle mesh Ewald method" *J. Chem. Phys.* **1995**, *103*, 8577-8593.

[6] S. Nosé, "A unified formulation of the constant temperature molecular dynamics methods" *J. Chem. Phys.* **1984**, *81*, 511-519.

[7] W. G. Hoover, "Canonical dynamics: Equilibrium phase-space distributions" *Phys. Rev. A* **1985**, *31*, 1695-1697.

[8] W. Humphrey, A. Dalke, K. Schulten, "VMD: Visual molecular dynamics" *J. Mol. Graph.* **1996**, *14*, 33-38.

[9] S. Pronk, S. Páll, R. Schulz, P. Larsson, P. Bjelkmar, R. Apostolov, M. R. Shirts, J. C. Smith, P. M. Kasson, D. van der Spoel, B. Hess, E. Lindahl, "GROMACS 4.5: a high-throughput and highly parallel open source molecular simulation toolkit" *Bioinformatics* **2013**, *29*, 845-854.